

# Metal Abundances in a Damped Ly $\alpha$ System Along Two Lines of Sight at $z = 0.93$ <sup>1</sup>

Sebastian Lopez<sup>2</sup>, Dieter Reimers<sup>3</sup>, Michael D. Gregg<sup>4,7</sup>, Lutz Wisotzki<sup>5</sup>, Olaf Wucknitz<sup>6</sup>,  
and Andres Guzman<sup>2</sup>

## ABSTRACT

We study metal abundances in the  $z = 0.9313$  damped Ly $\alpha$  system observed in the two lines-of-sight, A and B, toward the gravitationally-lensed double QSO HE0512–3329. Spatially resolved Space Telescope Imaging Spectrograph spectra constrain the neutral-gas column density to be  $N(\text{H I}) = 10^{20.5} \text{ cm}^{-2}$  in both A and B. UV-Visual Echelle Spectrograph spectra (spectral resolution FWHM =  $9.8 \text{ km s}^{-1}$ ) show, in contrast, significant line-of-sight differences in the column densities of Mn II and Fe II; these are not due to observational systematics. We find that  $[\text{Mn}/\text{H}] = -1.44$  and  $[\text{Fe}/\text{H}] = -1.52$  in damped Ly $\alpha$  system A, while  $[\text{Mn}/\text{H}] -0.98$  and  $[\text{Fe}/\text{H}] > -1.32$ , and possibly as high as  $[\text{Fe}/\text{H}] \approx -1$  in damped Ly $\alpha$  system B. A careful assessment of possible systematic errors leads us to conclude that these transverse differences are significant at a  $5\sigma$  level or greater. Although nucleosynthesis effects may also be at play, we favor differential dust-depletion as the main mechanism producing the observed

---

<sup>1</sup>Based on observations with the NASA/ESA *Hubble Space Telescope*, obtained at the Space Telescope Science Institute, which is operated by the Association of Universities for Research in Astronomy, Inc., under NASA contract NAS 5-26555. Also based on data obtained at the ESO Very Large Telescopes, program 70.A-0446(A).

<sup>2</sup> Departamento de Astronomía, Universidad de Chile, Casilla 36-D, Santiago, Chile.

<sup>3</sup> Hamburger Sternwarte, Gojenbergsweg 112, D-21029 Hamburg, Germany

<sup>4</sup> Physics Department, University of California, Davis, CA 95616

<sup>5</sup> Astrophysikalisches Institut Potsdam, An der Sternwarte 16, D-14482 Potsdam, Germany

<sup>6</sup> Institut für Physik, Universität Potsdam, Am Neuen Palais, D-14469 Potsdam, Germany

<sup>7</sup>Institute of Geophysics & Planetary Physics, Lawrence Livermore National Laboratory, Livermore, CA 94550

abundance gradient. The transverse separation is  $5 h_{70}^{-1}$  kpc at the redshift of the absorber, which is also likely to be the lensing galaxy. The derived abundances therefore probe two opposite sides of a single galaxy hosting both damped Ly $\alpha$  systems. This is the first time firm abundance constraints have been obtained for a single damped system probed by two lines-of-sight. The significance of this finding for the cosmic evolution of metals is discussed.

*Subject headings:* cosmology: observations — galaxies: abundances — intergalactic medium — quasars: absorption lines — quasars: individual (HE0512–3329)

## 1. Introduction

Measuring metallicities with 10% precision in high- $z$  damped Ly $\alpha$  systems (e.g., Prochaska & Wolfe 2002) has become a standard technique for tracing chemical evolution in neutral gas over a large fraction of a Hubble time. Surveys of damped Ly $\alpha$  systems (DLAs) contrast observations with models of chemical evolution, attempting to understand the nature of the objects hosting the absorbing clouds and to assess the degree of metal enrichment of gas in high redshift galaxies. The anticipated increase of  $[M/H]$  with cosmic time has become apparent only recently with the dramatic increase in sample size over the last few years (Prochaska et al. 2003a). However, this evolutionary trend is hidden by a considerable scatter in  $[M/H]$  of  $\approx 1$  dex<sup>1</sup>, that is seen at every epoch from  $z = 5$  to  $z = 0$ . The observed cosmic abundance spread at a given epoch is attributed to two distinct effects: (1) lines of sight to background QSOs probe a single location in DLAs at a random impact parameter, so gradients in DLAs will produce different abundances and dust-to-gas ratios, and (2) DLAs arise in a variety of galaxy types with different star formation and enrichment histories, as observed at low redshift (e.g., Boisse et al. 1998; Rao et al. 2003). Adding to the scatter, the overall census of DLAs might be biased toward lower metallicities because QSOs in front of very dusty and metal-rich absorbers might be missed entirely by optical surveys (e.g., Pei, Fall & Bechtold 1991; but see Ellison et al. 2001).

DLAs probed by two or more lines-of-sight offer a way to test these theories of the observed scatter in  $[M/H]$  while also further probing the nature of DLAs. The small impact parameters involved make gravitationally lensed QSOs the ideal tool for studying DLAs this way. The number of lens systems at high redshift, however, is small and so also the number of intervening DLAs (Le Brun et al. 2000; Smette, Claeskens, & Surdej 1997). The

---

<sup>1</sup>In the usual convention of  $[M/H] \equiv \log(M/H) - \log(M/H)_{\odot}$

relative faintness of QSOs and the small separations on the sky make spatially resolved, high-resolution spectroscopy challenging, and from the few cases studied, no separate DLA abundances have been obtained (Smette et al. 1995; Zuo et al 1997; Lopez et al. 1999; Kobayashi et al. 2002; Churchill et al. 2003; Ellison et al. 2004a).

In the course of a Hubble Space Telescope imaging snapshot survey using STIS to search for small separation gravitationally lensed quasars, HE0512–3329 was discovered (Gregg et al. 2000). This system is a double image QSO at  $z_{em} = 1.58$  with a separation of just  $0''.644$ . The extinction and microlensing properties have been investigated by Wucknitz et al. (2003; hereafter ‘Paper I’). In this work, we focus on the metal abundances in the DLA observed along the two lines of sight toward HE0512–3329. The position angle of the two point sources is  $17^\circ$  N to E, with the brighter component (hereafter ‘A’) to the North. The small separation of HE0512–3329 makes ground-based spectroscopy extremely challenging and since achieving cleanly separated spectra is crucial for the present study, a good fraction of this paper is devoted to a description of data reduction (§ 2) and possible systematic effects (§3). The derived abundances at  $z = 0.9313$  are presented in § 4, again with careful consideration of possible systematics. The results are discussed in §5, and a summary is given in §6. We adopt a  $H_0 = 70 \text{ km s}^{-1} \text{ Mpc}^{-1}$ ,  $(\Omega_M, \Omega_\Lambda) = (0.3, 0.7)$  cosmology.

## 2. Observations and Data Reduction

### 2.1. HST STIS observations

Spatially resolved spectra of HE0512–3329 A and B were obtained with the Space Telescope Imaging Spectrograph (STIS) in first-order grating spectroscopic mode using G230L with the MAMA detector and G430L with the CCD. Details of the observations and data reduction are found in Paper I. The wavelength coverage is 1570 to 5700 Å at a spectral resolution of 3.3 Å in the blue and 4.1 Å in the red, or  $\sim 300 \text{ km s}^{-1}$ . The signal-to-noise is  $S/N \sim 30$  in all regions of interest. This resolution and  $S/N$  are not high enough to determine column densities of metal species, whose absorption lines are only a few  $\text{km s}^{-1}$  wide, but it is quite suitable for measuring the H I column density from the  $z = 0.93$  damped Ly $\alpha$  line observed at  $\lambda = 2350 \text{ Å}$ . The  $N(\text{H I})$  is needed to measure the gas metallicity.

### 2.2. VLT UVES observations and Data Reduction

HE0512–3329 was observed using the VLT UV-Visual Echelle Spectrograph (UVES) on the nights of January 2 and 3 2003. The spectra of both QSOs were acquired simultaneously

by aligning the slit with the 2 images. This was judged the best way to quantify the amount of cross-talk between the partially resolved spectra. Since Paranal median seeing values are critically close to the separation between QSO images, service mode was preferred (with its associated caveats, see below). The dichroic '390 + 564' setup was used, which covers 3600 – 4800 Å in the blue arm, and 4600 – 7500 Å in the red one. Eight 3000 seconds exposures were obtained, with seeing monitor values ranging from 0".6 to 0".9. The slit width was 1".0 and the pixel scale is 0".18 in the red CCD, but only 0".25 in the blue. Under these circumstances, extraction of cleanly separated spectra becomes challenging.

To obtain separate spectra of HE0512–3329 A and B, we used our own reduction pipeline to extract spectra of multiple objects in echelle data. The algorithm is based on a simultaneous PSF fit to each of the seeing profiles with consideration of pixel variances. The fits are performed twice: first allowing all PSF parameters to vary, then constraining PSF width and position by modelling them with low-order polynomials along the spectral direction. The extracted flux is defined by the synthetic profiles, and a  $1\sigma$  flux error array results from propagation of errors (Lopez et al. 1999). In HE0512–3329, the spatial profile was found to be well-represented by a Moffat function (Moffat 1969) with best-fit index parameter  $\beta = 2.5$  (see Fig. 1a).

Besides spatial resolution, low S/N is also a problem in the present UVES data. On-chip binning in the spectral direction only could not be carried out because this was not offered in service mode. Attempts to extract the QSO spectra from the unbinned data were unsuccessful, resulting in large flux residuals, leading us to bin the data by 4 pixels in the dispersion direction; the data have an initial FWHM= $\sim 6$  pixels, so there is margin enough for rebinning. To this end, the echelle orders were first 'unbent'. Fortunately, the use of gratings as cross-dispersers makes UVES data free from distortions in the spatial direction (no emission line 'tilts'), so the order rectification is not critical. Rectification was done with our own script, which traces the echelle orders with a Hough transform (Ballester 1994), re-samples the data in the spatial direction, computes the distance (in fractions of a pixel) to the center of the order definition, and re-allocates pixels with respect to a new, straight order definition. The rectified orders could then be re-binned  $\times 4$  along the spectral direction—now aligned with the CCD rows—thus increasing the S/N without distorting the spatial profile. The goodness of the treatment is illustrated in Fig. 1a, where the spatial profile of the standard star keeps its symmetry and Moffat-function-like form after the two processes.

Even at the improved S/N, the closeness of the two objects did not allow us to robustly determine a PSF width from global fits along the orders. Instead, this parameter (the actual seeing) was obtained from single-profile fits at wavelengths where one of the QSOs is completely absorbed by saturated  $z = 0.9313$  Mg II (Fig. 1b). The spatial separation between

QSO profiles was held fixed at  $0''.644$ , as determined from the space-based observations.

We found that the extracted spectrum of QSO A does not reach zero at the position of Mg II where we expect totally black absorption. One possible explanation for this residual is emission by the lensing galaxy at  $z = 0.93$ . To explore this, we averaged columns all the way along the absorption troughs – some tens of pixels – to obtain an averaged QSO profile (the rectified orders permit this operation). Up to 10% flux excess is present to the North of *both* QSOs. This PSF asymmetry is barely apparent in Fig. 1b [although the Figure shows just one column], and, although it explains the residual flux in QSO A, it seems to exclude the possibility that the excess is from the lensing galaxy (this is because any emission excess between the two QSO images would appear to the North of QSO B only). The extracted spectra were corrected by subtracting a pedestal at the level of up to 10% of the QSO B flux. The possible effect of this correction on absorption line parameters will be considered below.

Finally, to wavelength calibrate the extracted orders, exactly the same pre-processing was applied to the Th-Ar exposures. The final wavelength solution is accurate to rms  $\sim 1/7$  pixel. Before coadding orders, the spectra were rebinned to a common vacuum-heliocentric scale with pixel size of  $0.0994 \text{ \AA}$ . The final spectral resolution in the coadded spectra is FWHM  $\sim 9.7 \text{ km s}^{-1}$  ( $\sim 2$  binned pixels), and the final S/N per pixel is  $\approx 35 - 40$  for both A and B. Finally, the coadded orders were normalized directly by simultaneously dividing out the response function and QSO continuum. The continuum was estimated independently in A and B by fitting cubic splines through featureless spectral regions.

Unfortunately, a proper extraction of the blue-arm spectra was impossible given both the too poor spatial sampling and the lack of absorbed regions, needed to characterize the PSF. The final, usable, wavelength coverage is 4620 to 5600  $\text{\AA}$ .

### 3. Column Densities and Assessment of Systematic Errors

We used two methods to obtain column densities: the apparent optical depth method (AODM; Savage & Sembach 1991) and Voigt profile fitting. The fits were performed with the MIDAS package FITLYMAN (Fontana & Ballester 1995). While both methods offer similar results for weak transitions, strong blending is more reliably assessed by profile fitting. Only metal lines believed to be non-saturated were fitted (see below). Oscillator strengths,  $f$ , were taken from the new compilation by Morton (2000), and solar abundances from Grevesse & Sauval (1998).

While the UV STIS spectra are necessary for determining  $N(\text{H I})$ , accurate determi-

nation of the metal abundances requires the much higher spectral resolution provided by UVES. These two datasets suffer respectively from two possible systematic effects: bad continuum estimate, and cross-talk between UVES spectra. Since the main goal of the present study is to detect possible line-of-sight differences in the absorption line parameters, in the following we describe in detail these sources of error.

As a zeroth order approach we compare the reduced UVES spectra with the STIS data, which we assume to be fully resolved spatially. In Fig. 2 we show a comparison between the spectra redwards of the quasar Ly $\alpha$  emission; the high resolution data have been smoothed and rebinned to STIS specifications. A 5 Å shift was applied to the HST spectra to match the UVES vacuum-heliocentric wavelength scale (in the STIS acquisition images we found an offset from the image center of about 2 pixels, which, given the wide slit used, would correspond to a shift in the dispersion direction of  $\sim 5$  Å). We note a good match in the displayed transitions, which supports a proper extraction of the UVES spectra.

Most of the lines detected in the STIS spectra are actually saturated, and so this makes it impossible to fairly compare column densities of A and B. Indeed, unsaturated transitions are lost in the noise of the STIS data. We attempted a comparison of equivalent widths between (unconvolved) UVES and STIS non-saturated lines; while consistency is found in a few cases, most of these lines are not detected at the  $3\sigma$  significance level in the STIS spectra. Thus, a comparison of STIS and UVES data serves as a valuable consistency check between the ground and space-based observations; however, even flux discrepancies in the UVES data as high as 10%, or equivalent width differences as high as 30% in non-saturated lines would be impossible to detect at the modest S/N and spectral resolution of the STIS data.

To assess the impact of possible cross-talk effects on column densities, we computed equivalent widths of several *weak* lines in the UVES spectra, typically of  $\sim 30$  mÅ, observed. Mock echelle orders were then created in which 10% of the –non-normalized– flux of one QSO was respectively added to and subtracted from the other QSO. The mock spectra were renormalized, and equivalent widths of the same absorption lines were re-computed. We found typical deviations of the order  $\sim 8\%$  in equivalent width. For intrinsically strong transitions, e.g., Fe II  $\lambda 2586$ , this equivalent width corresponds to  $N \approx 5 \times 10^{12}$  cm $^{-2}$ , and the differences translate into 0.04 dex deviations. We will assume this is the column density uncertainty that propagates from the UVES extraction.

Finally, besides internal errors in the fit we have to account for another possible systematic error, namely the continuum definition. While not a problem in the UVES data, the continuum at the damped Ly $\alpha$  lines might be affected by Ly $\alpha$  forest interlopers. To account for this, we performed a series of fits on spectra normalized by different QSO continua. The

modified continua were artificially displaced by  $1\sigma$  from the flux error array. The new fits led to H I column densities that differed by  $\sim 0.07$  dex from the original values. Since internal fit errors were 0.03 dex, and since both errors are uncorrelated, we will assume a final 0.08 dex uncertainty in the H I measurements.

#### 4. Abundances in the Damped Ly $\alpha$ System at $z = 0.9313$ .

We next describe our measurements of column densities and abundances in DLA A and B. Table 1 summarizes the results of this section.

##### 4.1. H I in DLA A and B

The H I column density comes from Ly $\alpha$  as observed in the STIS spectra (Fig. 3; unfortunately, the flux at the position of Ly $\beta$  is absorbed in either sightline by an optically thick Lyman-limit system at  $z = 1.137$  – see paper I). To obtain  $N(\text{H I})$  we fitted Voigt profiles to the STIS spectra. The profiles and  $1\sigma$  deviations are shown in the Figure. Inspection of panel B indicates blended absorption by H I redwards of  $z = 0.9313$ , which we have included in the fit of Ly $\alpha$  B. Fortunately, the STIS resolution/signal-to-noise enables a fairly robust fit of the two velocity components. Furthermore, the quite well constrained line centroids (same results are obtained if  $b$  is held fixed at different values) are separated by a velocity difference  $\Delta v = 1043 \pm 100 \text{ km s}^{-1}$ , which pretty much matches the  $\Delta v = 960 \text{ km s}^{-1}$  between the stronger components of DLA B and a strong Mg II system observed at  $z = 0.9366$  in the UVES spectrum. The fits yield  $\log N(\text{H I}) = 20.49$  (A) and 20.47 dex (B), with internal fit errors of 0.03 dex in both cases, and so the same values in A and B. Significantly, a single-line fit of Ly $\alpha$  B yields the same  $N(\text{H I})$  when only the blue wing of the line is used to constrain the fit.

##### 4.2. Metals in DLA A and B

Fig. 4 shows the UVES spectra of A (left panels) and B in a velocity scale relative to  $z = 0.9313$ . Sightline A intercepts 7 clouds or velocity components from  $v = -129$  to  $v = 126 \text{ km s}^{-1}$ , with  $\Delta v \sim 255 \text{ km s}^{-1}$ . In sightline B we observe the bulk of absorption to be concentrated in 4 components around  $-130 \text{ km s}^{-1}$ , but there are also fifth and sixth weak components, readily seen in Mg II and Fe II at  $+80$  and  $+140 \text{ km s}^{-1}$ . The total velocity span is  $\approx 320 \text{ km s}^{-1}$ . These kinematic structures are similar to those ones observed

in higher-redshift DLA systems. A study of the kinematics of this system will be offered in a forthcoming paper. In the following, we treat each sightline separately.

#### 4.2.1. DLA A

As shown in Fig. 4 the only non-saturated transitions available in the A spectrum are Mn II  $\lambda 2576, 2594$ , Fe II  $\lambda 2586$ , and probably Mg I  $\lambda 2852$ . Below we assess the non-saturation character of the 2586 line. The Mn II lines are blend-free. Integrating the 2576 line in the range  $v = -170, 150$  (this range was selected to include all Fe II components) yields an observed equivalent width of  $W_\lambda = 0.13 \text{ \AA}$ , and an AODM column density of  $\log N(\text{Mn II}) = 12.55 \text{ cm}^{-2}$ . A Voigt-profile fit of the two transitions, on the other hand, yields a total column density (3 velocity components) of  $\log N(\text{Mn II}) = 12.58 \pm 0.03 \pm 0.04$  (internal fit error and systematics). We note in passing that the good fit of both transitions reflects a minimal degree of extraction systematics. We will adopt a conservative value of  $\log N(\text{Mn II}) = 12.58 \pm 0.05$ , which error considers possible cross-talk systematics described above. Based on this value and the H I column density, the metallicity of DLA A is  $[\text{Mn}/\text{H}] = -1.44 \pm 0.09 \text{ dex}$ .

The Fe II  $\lambda 2586$  and Mg I  $\lambda 2852$  were fitted simultaneously with 6 velocity components (labeled in the  $\lambda 2586$  panel). In the stronger Fe II  $\lambda 2600$  transition more components are readily detected but will not contribute significantly in the fit of the 2586 line. We find  $\log N(\text{Fe II}) = 14.47 \pm 0.06 \pm 0.04$ . Thus, for DLA A we get  $[\text{Fe}/\text{H}] = -1.52 \pm 0.11 \text{ dex}$ , and  $[\text{Mn}/\text{Fe}] = 0.08 \pm 0.07$

Given the importance of the  $\lambda 2586$  transition for the present study, we must assess possible saturation in this line. As pointed out by Savage & Sembach (1991), hidden saturation of line components can be detected by comparing the apparent column density per unit velocity,  $N_a(v)$ , of transitions of the same species but with different  $f\lambda$ , where  $\lambda$  is the rest-frame wavelength. In particular, we are interested in finding out to which level the two main velocity components in  $\lambda 2586$  (2 and 3) might be saturated. To this end, the left-hand panel of Fig. 5 shows a comparison of the iron transitions available. As expected, the 2600 transition (with higher  $f\lambda$ ) yields systematically lower pixel column densities as a consequence of it being saturated. If we focus on components 1 and 6 – resolved and not saturated *in 2586* –, we note that the 2600 line reveals no saturation in 1, while traces of saturation are evident in 6. Therefore, for the present UVES data this is roughly the optical depth regime,  $\tau \sim 1.7$ , where hidden saturation becomes important. Since component 2 in 2586 peaks at this  $\tau$ , this line should be considered slightly saturated, and the integrated AODM column density in consequence slightly underestimated. An independent test of the



small saturation effect in  $\lambda 2586$  is made in the right-hand panel of Fig. 5, where we overplot a scaled  $N_a(v)$  obtained from the weak Mn II  $\lambda 2576$  line. Under the assumption of a nearly constant Mn II/Fe II ratio over this velocity interval, we expect both profiles to agree within uncertainties if the  $\lambda 2586$  is only slightly saturated. It can be seen that both profiles do show an overall similar shape, at least to an extent where the information on  $N_a(v)$  is not lost in the noise of the  $\lambda 2576$  line. As a consequence, we feel confident that the effect of saturation only marginally affects the  $N_{\text{AODM}}$  value of Fe II in Table 1, and that it might have completely been corrected in the adopted  $N_{\text{fit}}$ .

#### 4.2.2. DLA B

As shown in Fig. 4 the only non-saturated transitions available in the B spectrum are Mn II  $\lambda 2576, 2594$ . The 2594 line is blended with the  $z = 1.13$  Fe II  $\lambda 2344$  line. Integrating the 2576 line in the range  $v = -210, -80$  yields an equivalent width of  $W_\lambda = 0.33 \text{ \AA}$ , and an AODM column density of  $\log N(\text{Mn II}) = 12.99 \text{ cm}^{-2}$ . A Voigt-profile fit of the two transitions, on the other hand, yields a total column density (3 velocity components) of  $\log N(\text{Mn II}) = 13.02 \pm 0.01 \pm 0.04$ . Note that the synthetic profiles show readily slight discrepancies, which we believe are not due to inaccurate atomic data but instead can be attributed to cross-talk extraction problems. A fit of Mn II  $\lambda 2576$  only yields  $\log N(\text{Mn II}) = 13.00$ , which is within our estimate of those systematic errors. We will conservatively adopt  $\log N(\text{Mn II}) = 13.02$ . Based on this value, the metallicity of DLA B is therefore  $[\text{Mn}/\text{H}] = -0.98 \pm 0.09 \text{ dex}$ .

The two Fe II transitions in the UVES spectrum are saturated; therefore, from the integrated apparent optical depth we only get a quite conservative lower limit of  $\log N(\text{Fe II}) > 14.65$ , or  $[\text{Fe}/\text{H}] > -1.32 \text{ dex}$ , and  $[\text{Mn}/\text{Fe}] < 0.34 \text{ dex}$ . A Gaussian fit to the much weaker ( though saturated )  $\lambda 2374$  line in the STIS spectrum yields an observed equivalent width of  $W_\lambda = 1.33 \pm 0.30 \text{ \AA}$ , which translates into the same lower limit for  $N(\text{Fe II})$ . In a different approach to estimate the Fe abundance, we generated synthetic profiles of these two Fe II lines by using the same number of components,  $b$ -values and redshifts obtained from the Voigt-profile fits to the Mn II transitions. Fe II Doppler parameters in excess of those of Mn II are not physical. The Fe II column density was chosen to get  $[\text{Fe}/\text{H}](\text{B}) = [\text{Fe}/\text{H}](\text{A}) = -1.52$ . The resultant profiles are superimposed with dotted lines in the two Fe II B panels of Fig. 4. Comparing with the data, the absorption excess is evident; moreover, it cannot be accounted for by increasing  $b$  even by several  $\sigma_b$ 's, nor can it be the result of an extraction artifact. The Fe column density of the B profiles has to be further increased by  $\approx 0.4\text{--}0.5$

dex to match the data ( $[\text{Fe}/\text{H}] \approx -1.1 - -1.0$ )<sup>2</sup>. This analysis indicates that, first,  $[\text{Fe}/\text{H}](\text{B}) > [\text{Fe}/\text{H}](\text{A})$  without any doubt; and second, the excess metallicity in B *might* be in line with that for Mn II, so that  $[\text{Mn}/\text{Fe}](\text{A}) \approx [\text{Mn}/\text{Fe}](\text{B})$ .

## 5. Discussion

### 5.1. Metallicity at $z = 0.93$ and the DLA galaxy

There are currently only 5 measurements of metallicity in DLAs at  $z < 1$  (Prochaska et al. 2003a). The  $z = 0.9313$  DLA in HE0512–3329 adds an important value to the overall sample at an epoch for which models of chemical evolution can distinguish different kinds of galaxy morphologies (Calura, Matteucci & Vladilo 2003). The metallicity derived for DLA A,  $[\text{Fe}/\text{H}] = -1.52$ , is representative of the  $z \approx 1$  sample, and the data on Mn and Fe abundances either in A or B are consistent with a low-metallicity and dusty absorber, as we shall discuss below.

Because the galaxy hosting the  $z = 0.9313$  absorbers is also the likely lensing galaxy, DLA A and B then probe the ISM on two opposite sides and the impact parameters cannot be larger than  $2.5 h^{-1}$  kpc. These small distances are counterexamples to the claim that lines-of-sight close to DLA galaxies are missing from DLA samples due to dust obscuration (see discussion in Ellison et al. 2001). A further example is the  $z = 0.807$  QSO HS 1543+5921, which line-of-sight intersects the DLA galaxy—a low surface brightness galaxy at  $z = 0.009$ —at only  $0.5 h^{-1}$  kpc (Reimers & Hagen 1998; Bowen, Tripp, & Jenkins 2001), yet without any detectable reddening.

Deep imaging of DLA fields has uncovered an inhomogeneous population of gas-rich galaxies with a range of morphologies and luminosities (e.g., Le Brun et al. 1997). For HE0512–3329, Gregg et al. estimated the lens to be roughly consistent with an  $L^*$  galaxy. It is remarkable to find such a low-metallicity absorber so close to a luminous galaxy. Discrepancies between gas-phase and emission-line abundances have recently been studied by Ellison et al. (2004b).

---

<sup>2</sup>Alternatively, additional weak velocity components—detected in Fe II but not in Mn II—might also contribute to the extra absorption.

## 5.2. Two Damped Ly $\alpha$ Systems, One Reshift

The real value of HE0512–3329 as a DLA probe comes from its double nature. Although perhaps a rare situation, the dual sight-line abundances obtained here allow us to reach some important conclusions.

The present data on HE0512–3329 are consistent with transverse differences in *both* [Mn/H] and [Fe/H] at  $z = 0.9313$ . For Mn, this gradient amounts  $0.46 \pm 0.13$  dex (fit and systematic errors) on a spatial scale of  $\sim 5 h^{-1}$  kpc and with sightline A passing through the more metal-deficient gas-phase<sup>3</sup>. Our analysis shows that a similar gradient is present also in [Fe/H], although the observational uncertainties are larger.

Interestingly,  $[\text{Mn}/\text{Fe}](\text{A}) \approx [\text{Mn}/\text{Fe}](\text{B})$ , which, if not greatly affected by dust —see below—, suggests chemical uniformity across the lines of sight at much larger distances than probed before (Churchill et al. 2003; Ellison et al. 2004a) and in accordance with uniformity along the lines of sight (Lopez et al. 2002; Prochaska 2003b).

## 5.3. Dust

Abundance patterns observed in DLAs are a consequence of both nucleosynthetic yields and differential incorporation of atoms into dust grains in the DLA ISM. Being an Fe-peak element, Manganese shares a common origin with Fe; however, a manganese underabundance is expected from the nucleosynthesis odd-even effect (Truran & Arnett 1971), borne out by measurements of Galactic disk and halo star abundances (Lu et al. 1996 and references). On the other hand,  $[\text{Mn}/\text{Fe}] > 0$  in diffuse ISM clouds of the Galactic disk for all range of metallicities (Savage & Sembach 1996); this is because iron is more prone than Mn to dust depletion, and consequently underabundant in the gas phase.

Our analysis of DLA A indicates  $[\text{Mn}/\text{Fe}] = 0.08 \pm 0.07$ . This ratio, consistent with solar, is among the highest of all [Mn/Fe] ratios at every redshift (Ledoux et al. 2002). Ledoux et al. have investigated in detail dust depletion effects on Mn; in particular they have noted a correlation of [Mn/Fe] with metallicity, which they interpret as the link between nucleosynthesis yields in DLAs and abundances in halo stars. In this regard (see their Figure

---

<sup>3</sup>We have noted that both sightlines cross other absorbing clouds at several  $100 \text{ km s}^{-1}$ . In particular, the A spectrum shows a weak Mg II-Fe II system that is separated by  $400 \text{ km s}^{-1}$  from the DLA. Although such a large velocity span likely implies two separated objects, even inclusion of this system would have minimal impact ( $< 5\%$  in column density) on the abundances derived for DLA A. Thus, the [Mn/H] gradient cannot be explained by a particular choice of velocity components.

4) DLA A is a clear outlier, with manganese being far too abundant for  $[\text{Fe}/\text{H}] = -1.5$ . The only explanation for this high value is significant dust depletion in DLA A. Following the their trend of  $[\text{Mn}/\text{Fe}]$  with  $[\text{Zn}/\text{Fe}]$  (the dust-to-gas ratio) iron in DLA A might be depleted by as much as 0.8 dex.

We have not been able to accurately quantify  $[\text{Mn}/\text{Fe}]$  in DLA B, but the present data are consistent with a similar ratio as in DLA A. This solar ratio *might* be taken as evidence for dust also in B since all observed DLAs have underabundant Mn unless  $[\text{Zn}/\text{Fe}] > \sim 0.6$ , an established indicator of dust depletion. However, the cosmic scatter of  $[\text{Mn}/\text{Fe}]$  at  $[\text{Fe}/\text{H}] = -1$  is larger and there are some examples of high  $[\text{Mn}/\text{Fe}]$  even at low  $[\text{Zn}/\text{Fe}]$ . Furthermore, our derived lower limit on Fe/H translates into a potentially lower Mn/Fe ratio, more in line with the general trend of DLAs at the low-depletion end.

#### 5.4. Gradient in Metallicity?

Supposing that the  $[\text{Mn}/\text{Fe}]$  in both A and B implies homogeneously distributed dust, a real metallicity gradient appears at a first glance as an attractive explanation for the transverse differences in  $[\text{M}/\text{H}]$ . In nearby spirals metallicity gradients as a function of galactocentric radius are found in the range  $-0.04$  to  $-0.20$  dex  $\text{kpc}^{-1}$  (e.g., Vila-Costas & Edmunds 1992). That the two images of HE0512–3329 are of similar brightness and that the lens is probably the DLA galaxy under study both imply the absorbing regions must lie more or less equidistant from the galaxy center, not farther than  $2.5 h^{-1}$  kpc (the lensing galaxy has so far not been detected, so its exact location is undetermined). This is consistent with the similar H I in DLA A and B. A simple model of varying metallicity with radius, therefore, cannot explain the differences observed at similar impact parameters.

#### 5.5. Differential Dust Depletion/Reddening?

Alternatively, differential dust depletion offers a plausible explanation of the abundance differences. As stated above, in A there is dust depletion by a factor of  $\sim 3$ . We now suppose that, on the contrary, in B the depletion is minimal, which is still consistent with  $[\text{Mn}/\text{Fe}] \approx 0$  given  $[\text{M}/\text{H}] \approx -1$ . There is enough evidence that at least some DLAs are bound to rotating systems, so some sightlines should encounter DLAs in disk+halo configurations. One such examples have been found by Quast, Reimers & Baade (2004) in the  $z = 1.15$  DLA toward HE 0515–4414. The velocity components there cover the whole range of depletion patterns from Warm Halo ( $[\text{Cr}/\text{Zn}] = -0.5$  dex) to Warm Disk ( $-1.1$ ) observed in our galaxy. In

HE0512–3329, the abundance pattern of DLA A closely resembles that of the the Galactic Warm Halo (see Fig.6 in Savage & Sembach), with Mn and Fe depleted by a factor of 3–4. In consequence, the different Fe and Mn abundances can be explained by lines of sight crossing Warm Halo-like regions that are subject to distinct dust depletion factors, with DLA B being less dusty.

In this scenario, the observed differences of  $[M/H]$  in HE0512–3329, where M are refractory elements, become a different and direct confirmation for the hypothesis of dust-depletion in DLAs. Moreover, we would expect differential reddening between QSO A and B (Pei, Fall, & Bechtold 1991). Photometric data of HE0512–3329 (Gregg et al.) in fact show that extinction along the line of sight to QSO A is greater, although as pointed out in Paper I, a chromatic effect of microlensing could also be present. As a rough estimate,  $\log N(\text{H I}) = 20.5$  dex leads to an expected color-excess of  $E(B-V) = 0.06$  if dust is present. With an SMC type extinction curve we get  $E(1250-V)/E(B-V) = 14$  (this is the shortest reliable wavelength of the extinction curve), which gives  $A(\lambda_{\text{obs}} = 2400\text{\AA}) = 0.84$  mag for an extinction factor of 2.2. This agrees with the  $f_A/f_B$  ratio from the STIS spectra plus an additional contribution due to microlensing (Paper I). The underlying assumption here is that the dust responsible for the depletion of Fe in DLA A is the same as for the extinction, a reasonable approach since extinction in the UV is dominated by small dust grains like iron oxides (see Prochaska & Wolfe 2002 for a complete discussion).

Finally, one concern on the differential-dust hypothesis: high-redshift DLAs in general do not appear to produce significant dust-reddening (Murphy & Liske 2004). In consequence, either dust at  $z = 0.93$  is not the main agent of the differential reddening observed in HE0512–3329, or DLA A is not representative of the systems studied by Murphy & Liske.

## 5.6. Final Remark

Regardless of the extent to which dust-depletion is acting differentially to alter  $[\text{Fe}/\text{H}]$ , one key consequence of the sightline differences in HE0512–3329 is their connection to the cosmic spread in  $[\text{Fe}/\text{H}]$ . The present sample of metallicity measurements at all redshifts is distributed within  $[\text{Fe}/\text{H}] = 0, -3$  dex (see Prochaska et al. 2003a for the latest compilation). The overall spread is a consequence of a mild but readily noticeable evolution of metals over a Hubble time. Petinni et al. (1994), however, found that even sub-samples within narrow redshift bins show large scatter of more than 1 dex. This is not attributable only to dust-depletion ( $[\text{Zn}/\text{H}]$  vs.  $z$  shows a similar behaviour, and zinc is not depleted); different star formation histories must contribute to the inhomogeneity. Despite this, if the DLA in front of HE0512–3329 is representative of  $z \approx 1$  DLAs, then the present sample of DLA abundances

must be randomly biased by effects other than galaxy type, such as the specific evolutionary stage in a particular line of sight, perhaps a high recent SN rate, or high star-formation rate with many UV emitting stars, which in the case of DLA B may have inhibited dust formation. In the overall context this would mean that the "patchiness" of star formation in a given galaxy dominates which type of DLA we observe; furthermore, this stochastic ingredient could be more marked at higher redshifts, where mixing has had less time to occur. In conclusion, part of the cosmic scatter must be due to these local effects which cannot be studied comprehensively. Obtaining better-quality optical spectra of HE0512–3329 A and B, especially in the spectral region covering Zn II and Cr II transitions, could offer important diagnostics for our understanding of abundances in DLAs as a whole.

## 6. Summary

We have studied the damped Ly $\alpha$  system at  $z = 0.9313$  in front of QSO HE0512–3329. This system is particularly advantageous for new insights into DLA studies because it is probed by two lines of sight, most likely on opposite sides of the lensing galaxy. We have confirmed the damped nature of the system in the two lines of sight and obtained H I column densities with help of spatially resolved STIS spectroscopy. Then, in a second result, we have obtained column densities of Fe II and Mn II in both lines of sight from ground-based echelle spectroscopy. This DLA becomes only the sixth case at  $z < 1$  with measured metallicity. We have assessed and quantified the sources of systematic error in the column densities, given (1) the challenging character of the data reduction and (2) the small set of transitions that could be measured. We inspected in detail cross-talk effects in the echelle data, continuum estimates in the STIS data, and saturation effects in the reduced spectra. Armed in the end with a small set of Mn and Fe abundances in each of the sightlines, our third result is the discovery of significant differences,  $\sim 0.5$  dex in both [Mn/H] and [Fe/H], on a transverse scale of  $5 h^{-1}$  kpc, while [Mn/Fe] appears solar in both A and B. Our treatment of errors leaves no doubt that the gradient is real, and we have discussed two possible causes: different nucleosynthesis yields and differential dust-depletion. Regardless of what produces the gradient in this particular DLA, our finding offers a compelling explanation for the source of scatter in the observed evolution of metals in the neutral Universe.

We have benefitted from comments made by Sara Ellison, Cedric Ledoux, and Celine Peroux. We are also grateful to the anonymous referee for a very useful report. SL would like to also thank the ESO Scientific Visitor Program for supporting a pleasant stay at ESO Headquarters, where part of this work was done. SL also acknowledges support from the Chilean *Centro de Astrofísica* FONDAF No. 15010003, and from FONDECYT grant

N°1030491. OW is funded by the BMBF/DLR Verbundforschung under grant 50 OR 0208. Additional funding for this work was provided by NASA through grant number GO-9165 from the Space Telescope Science Institute, which is operated by AURA, Inc., under NASA contract NAS5-26555.

## REFERENCES

- Ballester, P. 1994 *A&A*, 286, 1011
- Boissé, P., Le Brun, V., Bergeron, J., & Deharveng, J.-M., 1998, *A&A*, 333, 841
- Bowen, D. V., Tripp, T. M., & Jenkins, E. B., 2001, *AJ*, 121, 1456
- Calura, F., Matteucci, F., & Vladilo G. 2003, *MNRAS*, 340, 59
- Churchill, C. W., Mellon, R. R., Charlton, J. C., & Vogt, S., 2003, *ApJ*, 593, 203
- Ellison, S. L., Yan, L., Hook, I. M., Pettini, M., Wall, J. V., & Shaver, P. 2001, *A&A*, 379, 393
- Ellison, S. L., Ibata, R., Pettini, M., Lewis, G. F., Aracil, B., Petitjean, P., & Srianand, R. 2004a, *A&A*, 414, 79
- Ellison, S. L., Kewley, L. J., & Mallén-Ornelas, G. 2004b, submitted
- Fontana, A., & Ballester, P. 1995, *The Messenger*, 80, 37
- Gregg, M. D., Wisotzki, L., Becker, R. H., Maza, J., Schechter, P. L., White, R. L., Brotherton, M. S., & Winn, J. N. 2000, *AJ*, 119, 2535
- Grevesse, N., & Sauval, A.J. 1998, *Space Sci Rev*, 85, 161
- Kobayashi, N., Terada, H., Goto, M., Tokunaga, A., 2002, *ApJ*, 569, 676
- Le Brun, V., Bergeron, J., Boissé, P., & Deharveng, J. M., 1997, *A&A*, 321, 733
- Le Brun, V., Smette, A., Surdej, J., & Claeskens, J.-F., 2000, *A&A*, 363, 837
- Ledoux, C., Bergeron J., & Petitjean, P., 2002, *A&A*, 385, 802
- Lopez, S., Reimers, D., Rauch, M., Sargent, W.L.W., & Smette, A. 1999, *ApJ*, 513, 598
- Lopez, S., Reimers, D., D’Odorico, S., & Prochaska, J.X. 2002, *A&A*, 385, 778

- Lu, L., Sargent, W. L. W., Barlow, T. A., Churchill, C. W., & Vogt, S. 1996, *ApJS*, 107, 475
- Moffat, A. F. J. 1969, *A&A*, 3, 455
- Morton, D. C. 2000, *ApJS*, 130, 403
- Murphy, M. T., & Liske J. 2004, *MNRAS*, 354, 31
- Pei, Y.C., Fall, S.M., & Bechtold, J. 1991, *ApJ*378, 6
- Pettini, M., Smith, L. J., Hunstead, R. W., and King, D. L. 1994, *ApJ*, 426, 79
- Prochaska, J. X., & Wolfe, A. M. 1998, *ApJ*, 507, 113
- Prochaska, J.X. & Wolfe, A.M. 2002, *ApJ*, 566, 68
- Prochaska, J. X., Gawiser, E., Wolfe, A. M., Castro, S., & Djorgovski, S. G. 2003a, *ApJ*, 595, L9
- Prochaska, J.X. 2003b, *ApJ*, 582, 49
- Quast, R., Reimers, D., & Baade, R. 2004, in preparation
- Rao, S., Nestor, D., Turnshek, D., Lane, W., Monier, E., & Bergeron, J. 2003, *ApJ*, 595, 94
- Rao, S., Nestor, D., Turnshek, D., Lane, W., Monier, E., & Bergeron, J. 2003, *ApJ*, 595, 94
- Reimers, D. & Hagen, H.-J. 1998, *A&A* 329, L25
- Savage, B. D., & Sembach, K. R. 1991, *ApJ*, 379, 245
- Savage, B. D., & Sembach, K. R. 1996, *ARA&A*, 34, 279
- Smette, A., Robertson, J. G., Shaver, P., Reimers, D., Wisotzki, L., & Kohler, Th., 1995, *A&AS*, 113, 199
- Smette, A., Claeskens, J.-F., & Surdej, J. 1997, *NewA*, 2, 53
- Truran, J. W. & Arnett, W. D. 1971, *Ap& SS*, 11, 430
- Vila-Costas, M. B., & Edmunds, M.G. 1992, *MNRAS*, 259, 121
- Wucknitz, O., Wisotzki, L., Lopez, S., & Gregg, M. D. 2003, *A&A* 405, 445 (Paper I)
- Zuo, L., Beaver, E. A., Burbidge, E. M., Cohen, R., D., Junkkarinen, Vesa, T., Lyons, R. W., 1997, *ApJ*, 477, 568





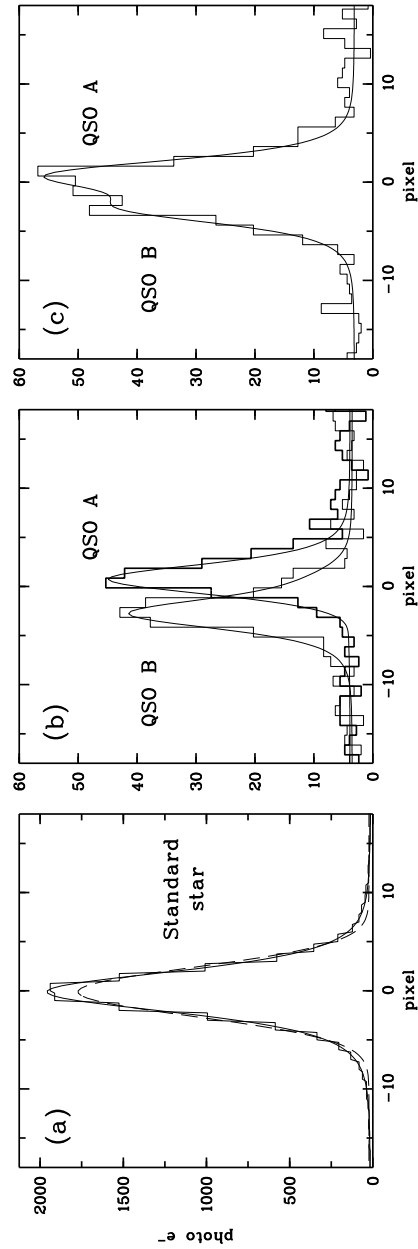


Fig. 1.— Spatial profiles in echelle orders of single exposures with UVES grating 564 (pixel size,  $0''.18$ ). The orders have been rectified and binned  $\times 4$  in the dispersion direction. (a) Standard star at seeing of  $0''.8$ . The dashed line is a best-fit Gaussian; the smooth line is a best-fit Moffat, taken to best represent the point-spread function. (b) HE0512–3329 A and B at two different wavelengths where black absorption by Mg II occurs in only one spectrum. Moffat best-fit profiles are overlaid. (c) HE0512–3329 A and B at an unabsorbed wavelength. In (a) and (b) the seeing was  $0''.63$  and the separation between QSO images is  $0''.64$ .

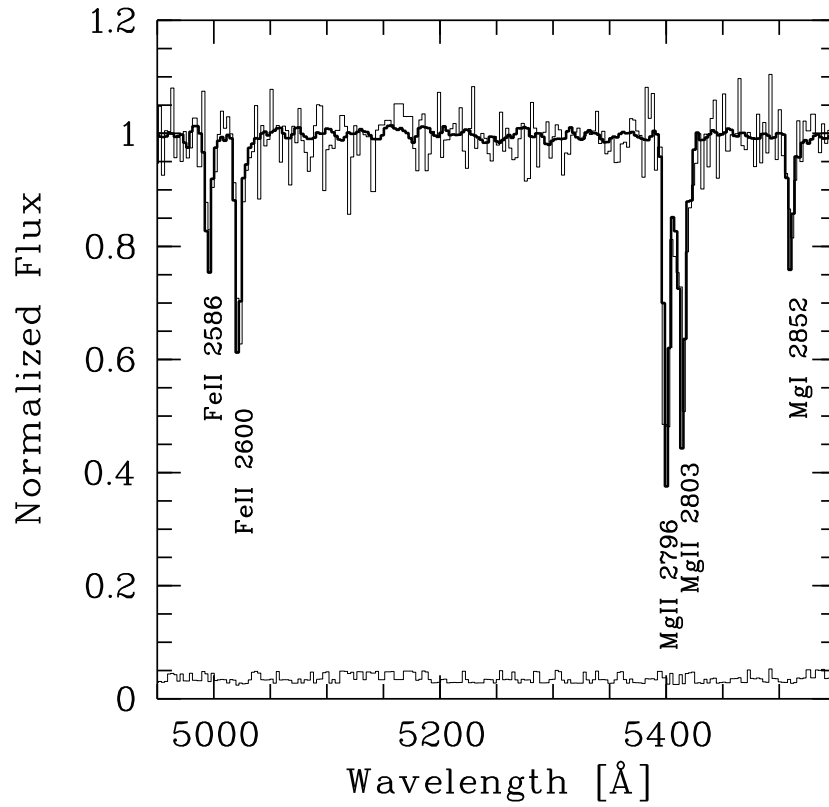


Fig. 2.— Comparison between STIS and UVES spectra of HE0512–3329 A redwards of Ly $\alpha$  emission. The UVES spectrum (thick line) was smoothed and rebinned to match the STIS specifications. Also shown is the  $1\sigma$ -error array of the STIS flux.

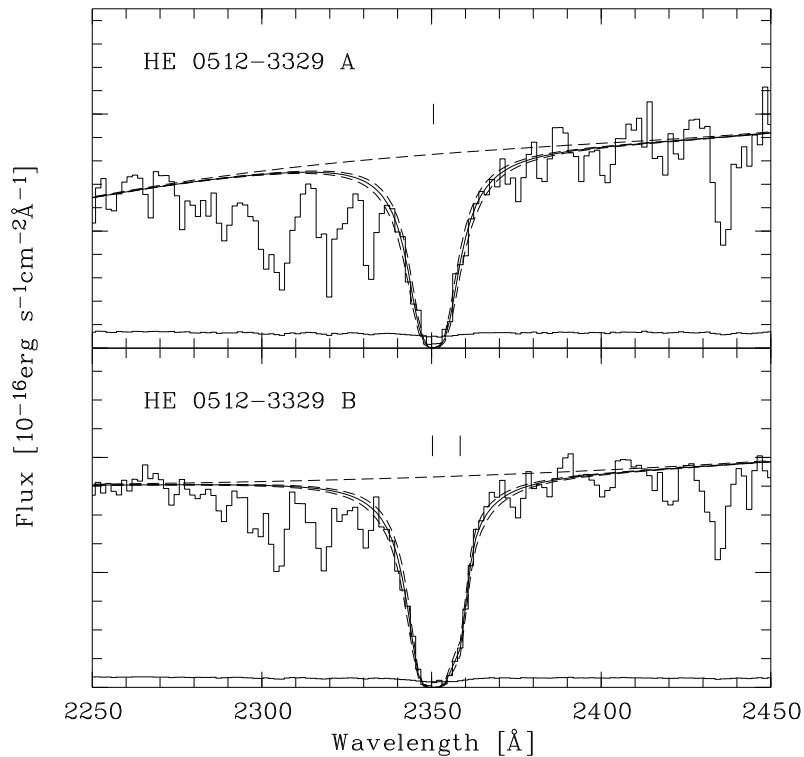


Fig. 3.— Portion of the HST STIS spectra of HE 0512-3329 A and B showing the two  $z=0.93$  damped Ly $\alpha$  lines (histogram). The dashed horizontal line displays the assumed QSO continuum. The smooth lines are Voigt profiles with  $\log N(\text{H I}) = 20.49$  (A) and 20.47 (B) dex, with 0.08 dex deviations indicated by the dashed curves. The tick marks indicate the fitted line centroids. In B, an additional HI line has been fitted with  $\log N(\text{H I}) = 18.8$  dex and Doppler parameter  $b = 20 \text{ km s}^{-1}$ . Although these values are uncertain due to the  $b$ -sensitivity on HI in this column-density regime, the uncertainty does not affect the  $\log N(\text{H I})$  of DLA B. The separation between the 2 tickmarks in B corresponds to 1043

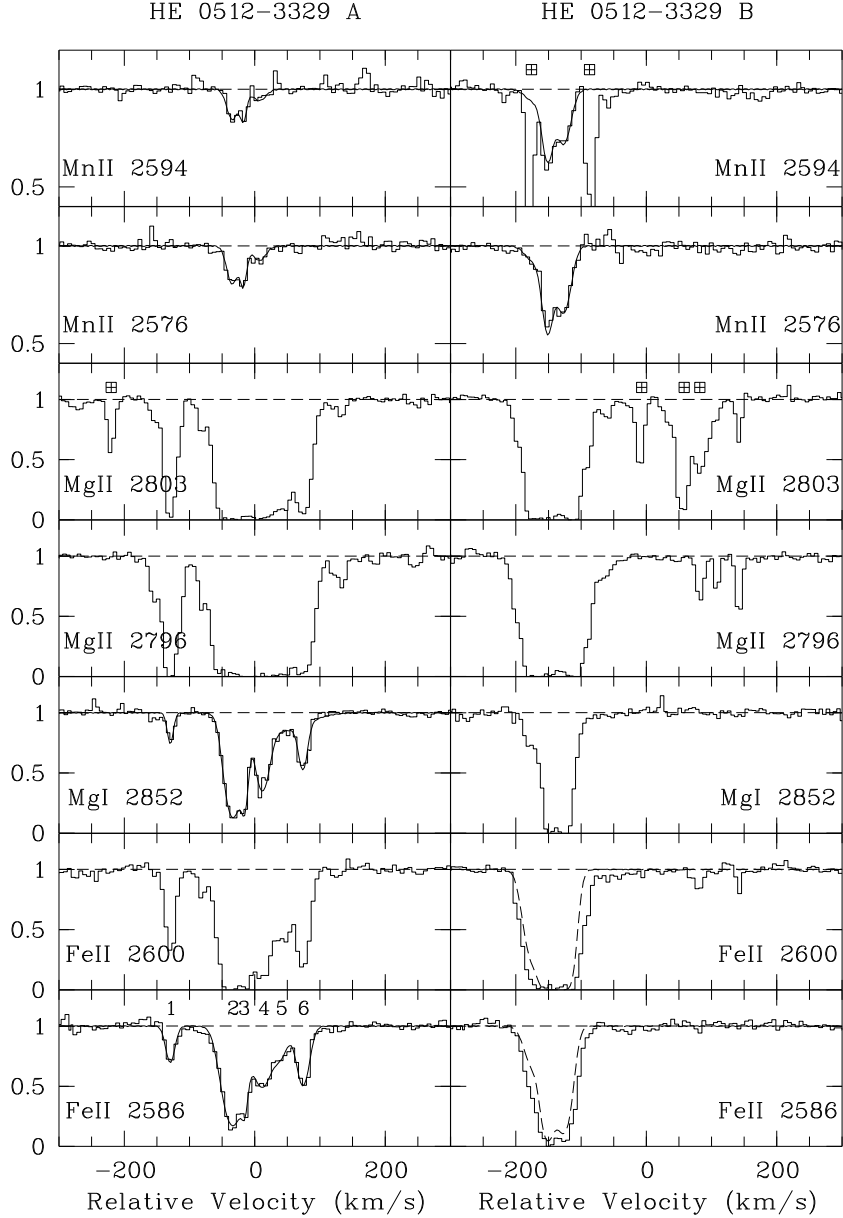


Fig. 4.— Absorption lines of the damped Ly $\alpha$  system observed in the UVES spectra of HE0512–3329 A (left panels) and B. The resolution is FWHM = 9.7 km s<sup>-1</sup> and the zero-point velocity corresponds to  $z = 0.9313$ . Overlaid are best-fit Voigt profiles whose parameters are listed in Table 1. Only lines believed to be non-saturated were fitted and the respective velocity components are labeled in the bottom-left panel. The dashed profiles in the two Fe II lines of B were generated with  $z$  and  $b$  from the Mn II(B) fits and a total column density  $\log N(\text{Fe II(B)}) = 14.45$  dex, which produces  $[\text{Fe/H}](\text{B}) = [\text{Fe/H}](\text{A})$ . Unrelated absorption features are marked with a crossed square.

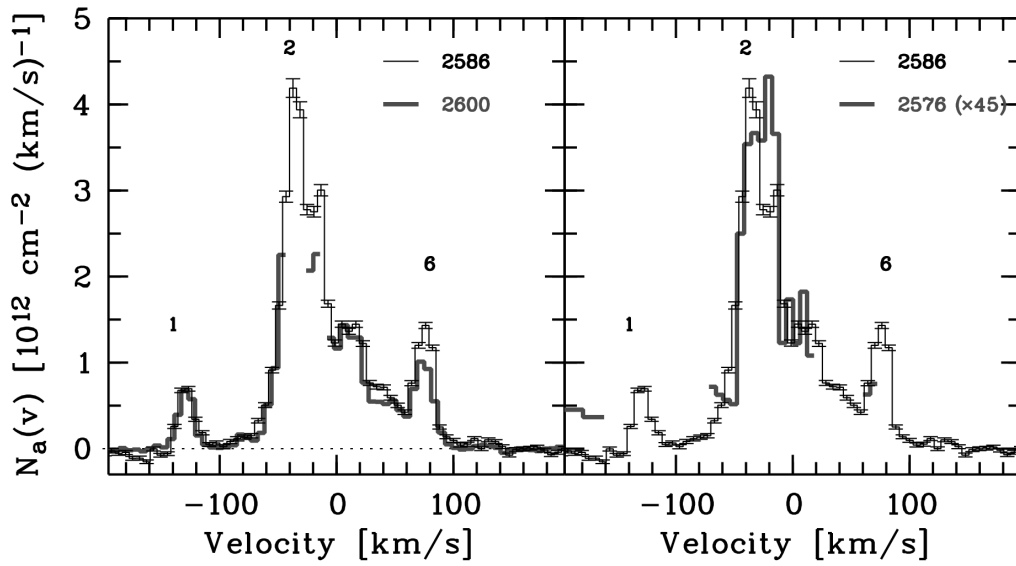


Fig. 5.— Apparent column density per unit velocity,  $N_a(v)$ , for the Fe II  $\lambda 2586$  transition (thin histograms) and for the Fe II  $\lambda 2600$  and the Mn II  $\lambda 2576$  transitions (thick histograms) in HE0512–3329 A. The  $\lambda 2576$  profile has been scaled up by a factor of 45. In both panels,  $N_a(v)$  was plotted only if the normalized flux of that pixel,  $f_i$ , fulfilled the condition  $2\sigma_i < f_i < 1 - 2\sigma_i$ , where  $\sigma_i$  is the error in  $f_i$ . Velocity components referred to in the text are labeled.

Table 1. Line Parameters in the  $z = 0.9313$  Damped Ly $\alpha$  System Toward HE0512–3329

Ion	$\lambda_0$	$f$	$W_\lambda$	HE0512–3329 A			$W_\lambda$	HE0512–3329 B		
				$\log N_{\text{AODM}}$	$\log N_{\text{fit}}$	[X/H]		$\log N_{\text{AODM}}$	$\log N_{\text{fit}}$	[X/H]
H I	1215.6701	0.4164	12.62	...	20.49±0.08	...	12.60	...	20.47±0.08	...
Mg I	2852.9642	1.8100	1.37	12.94±0.01	13.01±0.02	...	1.14	>12.95	...	...
Mg II	2796.3520	0.6123	3.75	>14.11	...	...	2.03	>13.90	...	...
Mn II	2576.8770	0.3508	0.13	12.55±0.01	12.58±0.03	-1.44±0.09	0.33	12.99±0.01	13.02±0.01	-0.98±0.09
Fe II	2594.4990	0.2710	0.09	14.41±0.01	14.47±0.06	-1.52±0.11	...	>14.65	...	>-1.32
	2586.6500	0.0691	1.33				1.23			

Note. — Column density errors are internal fit errors only; errors in [M/H] include fit and systematic errors.